MULTI-TEMPERATURE EMISSION AND ABUNDANCES IN THE HOT GASEOUS HALO

NASA Grant No. NAG5-9965

Final Report

For Period 1 October 2000 through 30 September 2003

Principal Investigator
Dr. Dong-Woo Kim

November 2003

Prepared for:

National Aeronautics and Space Administration
Goddard Space Flight Center
Greenbelt, MD 20771

Smithsonian Institution
Astrophysical Observatory
Cambridge, Massachusetts 02138

The Smithsonian Astrophysical Observatory
is a member of the
Harvard-Smithsonian Center for Astrophysics

The NASA Technical Officer for this Grant is Richard F. Mushotzky, 662.0, Goddard
Space Flight Center, Greenbelt, MD 20771

Attached is the final paper to be submitted to the Astrophysical Journal.

"XMM Observations of NGC 507: Super-solar Metal Abundances in the hot ISM"
Dong-Woo Kim and G. Fabbiano

Abstract

We present the results of XMM-Newton observations of NGC 507, a
dominant elliptical galaxy in a small group of galaxies. After
carefully considering various systematic effects on abundance
measurements, we report 'super-solar' metal abundances (both Fe and
a-elements) present in the hot ISM: ZFe = 2-3 times solar with an
observational limit of as high as 4 times solar inside the D25 ellipse
of NGC 507. This is the highest ZFe reported so far, and fully
consistent with those expected by the stellar evolution models where
heavy elements are enriched by both type II and Ia supernovae
ejecta. No unusual constraint either on the SNe rate or IMF is
required. Among various factors affecting the accurate abundance
measurement, we find that selecting a proper emission model is most
important. As opposed to the X-ray spectral data with limited s/n and
poor spatial/spectral resolution obtained in the previous missions,
the spatially resolved XMM spectra provide enough statistics to untie
the model-Z degeneracy and statistically require at least 3 emission
components in each concentric shell (2 thermal components representing
a finite range of kT in the hot ISM + 1 hard LMXB component). We show
that a simpler model (such as a two-component model) produce a much
lower best-fit ZFe. The abundances of a-elements (most accurately
determined by Si) is also found to be super-solar and its radio to Fe
is close to the solar ratio, suggesting a considerably contribution of
heavy elements from Type Ia SNe. We estimate ~70% of MFe in the hot
ISM originate from Type Ia.

We have also presented our preliminary/final results in the following
conferences.

- AAS HEAD meeting on Apr. 2002
        "XLF in Early Type Galaxies and its Implication on Measurement of
Metal Abundance"

- 2nd Korean Astrophysics Workshop on "Formation and Interaction of
Galaxies" in June 2002 (Pohang, Korea).
        "Chandra X-ray observations of Early Type Galaxies"

- AAS meeting on Jan 2003
        "XMM Observations of NGC 507: Overdensity of peripheral sources and
metal abundances in the hot ISM"

XMM-Newton Observations of NGC 507: Super-solar Metal Abundances in the Hot ISM

Dong-Woo Kim and Giuseppina Fabbiano

Smithsonian Astrophysical Observatory,
60 Garden Street, Cambridge, MA 02138

(November 25, 2003)

Abstract

We present the results of XMM-Newton observations of NGC 507, a dominant elliptical galaxy in a small group of galaxies. After carefully considering various systematic effects on abundance measurements, we report 'super-solar' metal abundances (both *Fe* and α-elements) present in the hot ISM: Z_{Fe} = 2-3 times solar with an observational limit of as high as 4 times solar inside the D_{25} ellipse of NGC 507. This is the *highest* Z_{Fe} reported so far, and fully consistent with those expected by the stellar evolution models where heavy elements are enriched by both type II and Ia supernovae ejecta. No unusual constraint either on the SNe rate or IMF is required. Among various factors affecting the accurate abundance measurement, we find that selecting a proper emission model is most important. As opposed to the X-ray spectral data with limited s/n and poor spatial/spectral resolution obtained in the previous missions, the spatially resolved XMM spectra provide enough statistics to untie the model-Z degeneracy and statistically require at least 3 emission components in each concentric shell (2 thermal components representing a finite range of kT in the hot ISM + 1 hard LMXB component). We show that a simpler model (such as a two-component model) produce a much lower best-fit Z_{Fe}. The abundances of α-elements (most accurately determined by *Si*) is also found to be super-solar and its radio to *Fe* is close to the solar ratio, suggesting a considerably contribution of heavy elements from Type Ia SNe. We estimate ~70% of M_{Fe} in the hot ISM originate from Type Ia.

2

1. Introduction

The abundance of heavy elements has been identified as one of the key quantities for our understanding of the evolutionary status of the hot ISM in terms of the supernova rate (Type Ia and II), initial mass function (IMF), mass ejection and onset of galactic winds (e.g., Renzini et al. 1993, Matteucci and Gibson 1995; Renzini 1997). Yet its measurement is difficult and controversial. This is mainly because different models result in considerably different best-fit value of metal abundances, i.e., *spectral degeneracy* between the applied emission model and the measured metal abundance. Because the accepted practice is to adopt the simplest possible model (relying solely on statistical errors), the previous X-ray spectra with limited signal-to-noise ratios and poor spatial/spectral resolution (possibly in conjunction with calibration uncertainties) were often fitted with a simple model (such as a single temperature thermal model), however the answer may not be astrophysically meaningful, because of the complexity of the X-ray sources (e.g., Kim, Fabbiano & Trinchieri 1992; Kim et al. 1996).

Fits of the ROSAT and ASCA data with single temperature thermal spectra (sometimes with a hard component to account for LMXBs) suggested a hot ISM almost totally devoid of metals (mostly *Fe*) in early-type galaxies (e.g., Awaki et al. 1994; Loewenstein et al. 1994; Davis and White 1996). This is significantly incompatible with the expected *Fe* abundance (a few times solar) based on the stellar evolution models (e.g., Arimoto et al. 1997) and has been known as *Fe-discrepancy*. On the other hand, several authors pointed out that more complex models allowed a metal content more in keeping with the stellar metallicities (e.g., Trinchieri et al. 1994; Kim et al., 1996; Buote and Fabian, 1998; Matsushita et al 2000), although could not well constraint Z_{Fe} because of the limited statistics. Kim et al. (1996) was the first to show that by statistically rejecting the simple model, the extremely low-Z model can be ruled out with the ASCA data of NC 4382, an X-ray faint S0 galaxy.

The recent results based on Chandra and XMM-Newton spectra of early type galaxies suggest the extremely low-Z can be statistically rejected and Z_{Fe} near the central region becomes close to (or slightly higher than) the solar value (Kim and Fabbiano 2003; Buote et al. 2002 and 2003; O'Sullivan et al. 2003). With high spatial resolution Chandra data, which allow to spatially exclude ~80 discrete sources, Kim and Fabbiano (2003) could convincingly exclude the possibility of extremely low metal abundances in the hot ISM of NGC 1399. Buote et al. (2002; 2003b) have reported a similar result by analyzing XMM-Newton spectra of NGC 1399 and NGC 5044 that the extremely low Z_{Fe} is excluded and Z_{Fe} near the center is slightly higher than the solar value. Similarly, O'Sullivan et al. (2003) reported a similar result in the galaxy group MKW4. However, the measured abundance is still not as high as that expected by the models. Also there are still confusing results: for example, O'Sullivan and Ponman (2003) report Z < 0.1 solar in 3 X-ray faint early type galaxies.

To unambiguously determine the abundances of heavy elements, we have performed a deep XMM-Newton observation of NGC 507, one of X-ray brightest early type galaxies

among the Einstein galaxy sample with $F_X \sim 10^{-11}$ erg sec^{-1} cm^{-2} (Fabbiano, Kim and Trinchieri 1992). NGC 507 has been extensively observed in X-rays: Einstein (Fabbiano et al. 1992), ROSAT PSPC (Kim and Fabbiano 1995; hereafter KF95), ROSAT HRI (Paolillo et al. 2003), ASCA (Matsumoto et al. 1997) and Chandra (Forman et al. 2002; Kraft et al. 2003). The ROSAT PSPC observation of NGC 507 revealed a cooler central region, i.e., a positive temperature gradient (KF95), typical of bright X-ray ellipticals or small groups of galaxies (e.g., Trinchieri et al. 1994; David et al. 1994; Trinchieri et al. 1997).

The previously reported metal abundances in the hot ISM of NGC 507 vary widely from 0.2 to a few times solar (e.g., Matsumoto et al. 1997; KF95; Buote and Fabian 1998). Using the high quality XMM-Newton X-ray spectra and taking into account various systematic effects (e.g., background spectra) and different methods of spectral analyses (e.g., de-projection, different ways of grouping heavy elements), we present accurate measurement of *Fe* and α-element abundances. In a subsequent paper, we will present the results of spatial analysis, including sub-structures of the hot ISM and the sources near the edge of the X-ray emitting region (in excess of the expected number of background serendipitous sources), which was first identified in the ROSAT PSPC observations (KF95). We note that because those surrounding sources are placed at the XMM-Newton aim point, we could obtain consistent background spectra determined locally at off-axis distances similar to the sources (see section 3).

This paper is organized as follows. In section 2, we describe the XMM-Newton observations and the data reduction methods. In section 3, we perform spectral fitting, considering various effects and measure the abundances of *Fe* and α-elements (Si, S, Mg and O). In section 4, we discuss the implications of our results in terms of the evolution of the hot ISM in conjunction with SN type Ia and II. Finally, we summarize our conclusions in section 5.

Through this paper, we adopt a distance $D = 70$ Mpc, based on the heliocentric velocity of 4934 km sec^{-1}, or z = 0.016 (Huchra et al. 1999) and $H = 70$ km sec^{-1}/ Mpc. At the adopted distance, 1 arcmin corresponds to 20.4 kpc, or $D_{25} = 3.1$ arcmin corresponds to 63 kpc.

2. XMM-Newton observations

NGC 507 was observed for 40 ksec on Jan. 15, 2001, with XMM-Newton MOS and PN (REF). We use SAS version 5.3 to reduce the data. We apply flag = 0 for all instruments and additionally pattern ≤ 4 for PN to exclude bad quality data. No significant background flare is seen during this observation. The effective exposure time is 34.1 ksec for each MOS and 26.6 ksec for PN. The X-ray spectra are extracted from each instrument, according to prescriptions in Snowden et al. (2002). We also use CIAO version 3.0 and XSPEC version 11.2 for further analysis.

4

Figure 1 shows the XMM-Newton X-ray (true color) image, made by combining mos1 and mos2 images and smoothing with gaussian σ=7.5″ with red for the soft band in 0.3-0.9 keV, green for the medium band in 0.9-2.5 keV and blue for the hard band in 2.5-8.0 keV. Figure 2 shows an unsmoothed image in the broad band (0.3-8 keV). Also marked in Figure 2 are the D_{25} ellipse of NGC 507 and regions where background spectra are extracted (see section 3).

The extended X-ray emission from the hot ISM is seen out to r=10′ (see also **KF95**) and also exhibits significant sub-structures. Also seen in the figures are a large number of sources present at the periphery of the hot ISM of NGC 507, as suggested by the ROSAT PSPC data (**KF95**). Identifying the nature of those sources was one of the motivations of this deep observation. We will present the results of source properties and spatial analysis of the hot ISM in a subsequent paper. In this paper we will concentrate on the X-ray spectral analysis of the hot ISM.

3. Spectral analysis

We extract spectra for each instrument (mos1, mos2 and pn) from several circular annuli, using xmmselect, available in sas v5.3. The annuli (with inner-outer radius = 0-1′, 1-2′, 2-3′, 3-5′, 5-7′ and 7-10′) are determined to be at least 1′ wide (considering the spatial resolution) and to contain at least 5000 counts in each radial bin from individual instrument after excluding background. We then group spectral bins to have at least 25 counts. Considering almost no X-ray emission from the hot ISM (and strong background emission) at E > 5 keV, we limit spectral fitting to the energy range of 0.3 – 5 keV. In each region, we determine redistribution matrix files (rmf) and auxiliary response files (arf) by rmfgen/arfgen available in sas v5.3. We note that the instrumental effect (possibly calibration uncertainty) becomes non-negligible at E > 5 keV, because the effective areas (given by arf) of MOS1 and MOS2 are slightly inconsistent and also the energy dependency of the telescope vignetting becomes significant at E > 5 keV.

For the solar abundance, we adopt the element ratios in Grevesse and Sauval (1998). Note that the new meteoric value for Fe is lower (by a factor of 1.48) than the commonly used value in Anders and Grevesse (1989). This change makes Z_{Fe} effectively increase by 50% from those previously determined, even with no other change.

We fit spectra from different instruments separately as well as jointly, to ensure whether any instrumental effect or calibration uncertainty affect the fitting results. All 3 instruments result in slightly different best-fit parameters, particularly for abundances of heavy elements. In general, the difference is not negligible, but consistent within the 90% error. On the other hand, the temperature (and its radial variation) is almost the same. We do not apply any artificial correction factor for different instruments to compensate the systematic error possibly caused by calibration uncertainties. Instead, we compare all 5 fitting results (individually for MOS1, MOS2 and PN and jointly MOS1 + MOS2 and MOS1 + MOS2 + PN) to show the amount of scatter (see Table 1).

To unambiguously determine metal abundances we thoroughly take into account various systematic effects. In Table 1, we summarize the goodness of spectral fitting (and the best-fit Z_{Fe} in the inner 2 regions) performed with various combinations of fitting options to illustrate their importance and the amount of scatter in the best-fit parameters. The best statistical results are obtained with the local background (**BKL**) and 3-component emission models (**3C**) (Fit1 and Fit7-10 in Table 1). The overall goodness of the fit is acceptable in these cases, with χ^2_{red} close to 1 (always < 1.2) with 500-2500 degrees of freedom. The template case (Fit1 in Table 1) consists of 5 different instrument combinations. In each case, the observed (local background subtracted) spectra extracted from 4 annuli (0-1′, 1-2′, 2-3′ and 3-5′) are simultaneously fitted with projected 3-dimensional models. Each model representing the emission from a 3-dimensional shell consists of 3 components: 2 soft thermal components (2 vmekal models where kT is free for a cooler one and fixed at 1.4 keV for a hotter one) and 1 hard component (7 keV Bremsstrahlung). All the heavy elements vary together, but independently in each shell and N_H is fixed at the Galactic value.

The remaining fitting results listed in Table 1 are obtained by varying 1 or 2 options from the template case. They include instruments (fitting individually or fitting jointly), 3 sets of background spectra (from the same observations or from blank-field data), emission models (2-components and 3-components), with/without de-projection (2-D and 3-D), different ways of grouping elements to vary together, N_H (fixing at the galactic value or free to vary), number of shells (or the outermost radius). We note that if not treated correctly, systematic errors could be larger than statistical errors. We will discuss each of them in detail.

3.1 Background Spectra

For extended sources, the accurate determination of background is often a non-trivial task. To confirm the accuracy of background spectra and to determine the effect of incorrect background subtraction, we have extracted 3 different sets of background spectra for each instrument. The first set (**BKL** in Table 1) is from the location close to the aim point, but 7-12 arcmin away from the center of NGC 507. In Figure 2, the red circle near the center of the field of view indicates the region of the local background (discrete sources are excluded). Because they are in a similar off-axis distance with the source location, we do not apply the correction for telescope vignetting. This is unique to our observation (albeit for a different purpose), because in most cases, the galaxy center is at the aim point. The second set (**BKE** in Table 1) is from the edge of the detector, 10-19 arcmin away from the center of NGC 507. The 3 blue circles located in the left and at the bottom of Figure 2 indicate the second background regions. We apply the vignetting correction based on effective areas given by arf at E < 5keV. The third set (**BKB** in Table 1) is from the blank field background data obtained from the XMM-Newton Science Operations Centre (Lumb 2002). We then scale the blank field data by the counts in 5-10 keV from the location of the first background region (close to the aim point). We also scaled the blank field spectra by the counts from the second background regions (i.e., at a large off-axis distance), but found considerably different, incorrect, scale factors. The discrepancy is

most likely due to the strong (and not well calibrated) energy dependency of spectral response functions at large off-axis distances. This brings a cautionary remark that the blank field data may not represent true background when scaled in high energies (> 5 keV) at large off-axis distances, although this is often the only available method in analyzing extended sources. See also Lumb (2002) for the discussion of energy-dependent field-to-field variation of the X-ray background.

The results with three different background spectra are compared Figure 3, where only MOS1 (left panel) and PN (right panel) data are plotted. The local background spectra (**BKL**) always give significantly better fit than the other two (compare Fit 1-3 in Table 1). The local background spectra (the top panel in Figure 3) work pretty well throughout the whole energy range, resulting in χ^2_{red} close to 1, and no localized deviation (e.g., near emission features or at lower/higher energies) is seen. In contrary, both background spectra taken at the edge (the middle panel) or from the blank field data (the bottom panel) produce poor fitting. Significant deviations near Mg (~1.5 keV) and Si (~2 keV) emission features are clearly seen in both cases. Also visible at higher energies are over-subtraction (in the middle panel) or under-subtraction (in the bottom panel). In both cases, χ^2_{red} ranges between 1.3 and 1.6 (see Table 1), corresponding to extremely low probability ($< 10^{-5}$).

The local background obtained at r = 7-12' (**BKL**) may contain some X-ray emission from the extended hot ISM (the hot ISM is extended out to 10'; **KF95**; Paolillo et al. 2003), but de-projecting X-ray emission effectively removes the extra emission as long as it is limited to r < 7'. Also note that adding or removing the outer shell(s) does not significantly change the results in the inner regions (see section 3.4).

3.2 Emission Models

The X-ray emission from early type galaxies can consist of many different emission components: a power-law component from the (low luminosity) AGN, hard X-ray emission from low-mass X-ray binaries (LMXB), soft thermal emission from the hot ISM and possibly remaining emission from the incompletely subtracted background sources. The AGN in the center appears to be low (this will be discussed in the subsequent paper). LMXBs will be the major hard X-ray emission component although we do not see them directly because typical LMXBs are too faint to be detected (see Section 5). The hot ISM of early type galaxies consists of multi-temperature gas. For NGC 507, it was already shown by ROSAT data that (to the first approximation) the temperature increases with increasing galactocentric distance (**KF95**). A mixture of multi-temperature (possibly inhomogeneous) gas likely co-exists even in a given (3-dimensional) shell at the constant distance (see more discussion in Section 5). Therefore, at least 3 emission components (2 thermal gas + 1 hard components) are required to fit the spectra from each annuli/shell, although the reality will be even more complex. [The residual background, which may be harder than LMXBs, could require another model component if incorrect background is used (as seen in Figure 3).] We also apply 2-component models (1 thermal gas + 1 hard components) to demonstrate the necessity of the 3rd component (see below).

We use vmekal for the thermal emission and Bremsstrahlung for the hard emission. Because individual LMXBs appear to exhibit a similar spectral property, based on the Chandra spectral data, we adopt $kT = 7$ keV for LMXBs (e.g., Kim and Fabbiano 2003; Irwin et al. 2003) and fix the temperature of the Bremsstrahlung component. In the 2-component fit, the temperature of the thermal component is free to vary, while in the 3-component fit (i.e., with 2 thermal components), we set the temperature of the softer thermal component to vary and fix that of the harder thermal component at 1.4 keV, because the average temperature varies from 1.4 keV at large galactocentric distance (i.e., ambient gas) to 0.6-0.8 keV near the center (see **KF95**; and also Table 1). Having the temperature of the harder thermal component set to vary does not improve statistics.

We compare the results of 3-componets vs. 2-components in Figure 4. We plot only MOS1 spectra, but the results from other instruments are similar. We find that significantly better fit with 3-components model than the 2-component models, indicating the presence of mixed temperature gas in a given shell (see Fit4 in Table 1). F-tests for 3-component models over 2-component models indicate extremely low probabilities to exceed the given F-statistics ($< 10^{-5}$). The localized deviations near the Fe peak (~1 keV) is clearly seen in the 2-component fit. This kind of deviation is reminiscent of spectral fitting with previous X-ray missions, where simplified models were often applied and extremely low Z with a tight error bar resulted (e.g., see Kim et al. 1996). The best-fit Z_{Fe} obtained in the 2-component fit is significantly lower that that of the 3-component fit (see section 4.1).

3.3 De-projection

Given the known radial temperature variation, we need to consider the projection effect on each spectra obtained in 2-dimensional annuli. To effectively de-project the observational data (assuming spherical symmetry), we use **project,** available in **xspec** v11.2, where 3-dimensional models (representing spectra from 3-dimensional shells) are projected into the 2-dimension plane and simultaneously fit to a set of spectra extracted from multiple annuli. We compare the results of 3-dimension (**3D**) vs. 2-dimension (**2D**) in Figure 4 (also see Fit5-6 in Table 1). In general, while the goodness of the fit is almost the same, the best fit-abundance is slightly higher in **3D** than in **2D** (but still within the statistical error). We note that the difference between 2-component and 3-component models is much more significant than that between **3D** and **2D**.

In this de-projection, we use 4 (up to 5′ from the center) 3-dimentional shells. As the extended emission continues at least 10′, we also use extra shells (in radius of 5-7′ and 7-10′). However, due to large uncertainties, particularly by incorrect background subtraction, fitting results vary significantly depending on the background spectra applied and become less reliable. However, the results within 5′ remain the same, regardless of using the outer shells.

8

3.4 Other effects

Given the limited statistics, it is not always possible to vary all the heavy elements independently. We try a few different groupings and set the group of elements vary together, to best determine Z_{Fe}, its ratio to α-elements, and ratios of a few individual elements with relatively strong emission feature. First, all elements vary together with Fe. Second, Si and S make one group and the rest elements form another, to separate α-elements (Si and S are the most prominent elements among them). Third, elements lighter than Ar make one group and the rest elements heavier than Ca another, again to distinguish α-elements and those mostly produced by SN Type Ia. Fourth, Si, S, O and Mg vary independently and the rest vary with Fe to individually determine heavy element abundances. In general, the goodness of the fit is almost the same, regardless of different grouping, but the best-fit abundances do vary (see Section 4.4).

It is expected that helium is mostly formed by the big bang. Some *He* can be synthesized in stars and later ejected into the ISM via stellar winds or mass loss during the last phase stellar evolution (REF). *He* does not have a strong feature in X-ray spectra. But, Z_{He} affects the best-fit metal abundance by altering the underlying continuum emission. This could be as much as XX % in Z_{Fe} in xxxx condition. We note that if *He* is set to vary as other elements (for example with Fe), Z_{Fe} will be even lower when it is sub-solar, while it becomes higher when super-solar.

Finally, we either fix N_H to be the galactic value (5×10^{20} cm^{-2}) or vary it freely (Fit7 in Table 1). The best-fit N_H is consistent with the galactic value in N sigma. We find that N_H often goes together with the amount of the hard component and affects Z_{Fe}, in a sense that more N_H and more hard component effectively reduce Z_{Fe}. We will discuss this *spectral degeneracy* in section 3.3 and 4.

4. Results

4.1. Temperatures of multi-component emission models

As shown in the ROSAT PSPC data (**KF95**), the temperature of the hot ISM decreases toward the center. To the first approximation, our results are consistent with the overall positive temperature gradient. However, the hot ISM within each 3-dimentional shell is not isothermal and a range of kT is required. As we apply two thermal components (in addition to a hard component) to best represent the actual mixture of multi-temperature gas, we can compare the radial variation of the relative contributions from the two components to assess the range of temperature and the degree of mixing. In Table 2, we list spectral parameters determined in each shell. Only results obtained by jointly fitting spectra from all instruments (MOSPN in Table 1) and those with good statistics (corresponding to Fit1 and Fit8-10 in Table 1) are listed. The temperature of the 1st soft component ranges from 0.6 to 0.8 keV with a relatively tight error of ~0.03 keV in the 90% confidence. (Throughout this paper, we quote the error determined in the 90%

confidence.) The X-ray flux ratio of the two thermal components measures the relative importance of cooler and hotter gas components (see Figure 5). In the innermost shell ($r <$ 20 kpc), the contributions from the two components are roughly equal, while in the 2nd shell ($r = 20 - 40$ kpc), they are 1:3 (less cooler component than in the central bin), clearly indicating that the hot ISM is not isothermal and the temperature is more complex than a simple radial gradient. In the outer shells ($r > 40$ kpc), the ratio drops to 1:12, as the ambient gas (at ~1.4 keV) dominates the X-ray emission. Note that the cooler component in the outer shells is still required, even though it is relatively small.

The 3rd (hard) component consists of ~7% of the total X-ray emission in the first 2 shell (i.e., within the optical galaxy, $r < 40$ kpc), which is consistent with the expected amount from LMXBs (see section 4). Its amount is undetermined in the 3rd shell ($r = 40 - 60$ kpc) (or possibly absent), while a non-negligible amount of the hard component is required in the 4th shell ($r = 60\text{-}100$ kpc). That may originate from background AGNs, or those similar to the excess sources detected at larger distances (this will be further discussed in paper II.)

In Table 2 (at the bottom), we also list the best-fit gas temperatures obtained with 2-component models (Fit4 and Fit6 in Table 1). Although the fit is poor (see also Figure 4), we can consider them as emission-averaged temperatures of the hot ISM, and also compare with the previous results. As measured in **KF95**, the temperature is ~1 keV near the center and increases to ~1.4 keV at the outskirts. Also we apply cooling flow models (vmkcflow in xspec). The low T is ~0.6 keV and the high T is ~1.4 keV near the center, but the fit is poor ($\chi^2_{red} \sim 1.5$). As reported in other early type galaxies and clusters (REF), we see no thermal emission from gas with $kT < 0.6$ keV, in any model used in this study.

We summarize (1) that the emission-averaged temperature of the hot ISM increases with increasing distance from the center (from ~1.0 keV to ~1.4 keV) and (2) that the hot ISM is not locally isothermal and require at least 3 emission components in each 3-dimensional shell, with more contribution from the cooler component ($kT \sim 0.6\text{-}0.8$ keV) toward the center and the emission from the ambient gas with kT~1.4 keV dominant at large radii.

4.2. Iron abundance

In the template case (Fit1 in Table 1), the best-fit Fe abundance is ~3 times solar in the center ($r < 1'$ or < 20 kpc) and ~2 times solar in $r = 20\text{-}40$ kpc and similar to (or slightly lower than) solar in $r > 40$ kpc. The acceptable range of Z_{Fe}, given by the statistical error in the 90% confidence is roughly ±1 solar in fitting spectra from individual instruments, or ±½ solar in jointly fitting spectra from multiple instruments. The maximum Z_{Fe} possibly given by the observation data could be as high as 4-5 times solar inside the D_{25} ellipse of the galaxy.

The results of super-solar Z_{Fe} and its radial variation (negative gradient) are quite robust, even if we consider systematic errors, which we measure by comparing various fitting

options. The 2-D fitting (i.e., without de-projection) produces a slightly lower Z_{Fe}, ~2 times solar in the center (Fit5). Varying N_H also reduces Z_{Fe} by a similar factor (Fit7). Different ways of grouping elements which vary together (Fit8-10 in Table 1) result in Z_{Fe} = 2-3 times solar in the center. Fit10 (**Z4** where Fe, Si, S, Mg, and O vary independently) appears to produce the lowest Z_{Fe} (see section 3.4 and 4), but still consistent with other results within the acceptable range. In this case (**Z4**), Z_{Fe} in the 2nd shell remains similar to that in the center (i.e., a shallow gradient). Considering all these various systematic effects, we conclude that Z_{Fe} is *super-solar* (~2 times solar or higher) in the D_{25} ellipse of the galaxy.

This conclusion is not affected by the uncertainty in background spectra. Although the fit with different background spectra is poor (see Fit2 and Fit3), we consider the difference in the best-fit parameters as a rough measure of uncertainties related with the background. Z_{Fe} still ranges between 2-4 times solar in both cases, consistent with our conclusion. Also we note that the super-solar *Fe* abundance measured in the central 2' bin will be least affected by the background uncertainties, because of the small contribution from the background X-ray emission to the central (small) region, while it is a more serious problem in the outer (large) region.

We note that the lowest Z_{Fe} is obtained with the 2-component model + no de-projection (Fit6). In this case, the best-fit Z_{Fe} is ~ solar, which would be ~0.6 solar with Anders and Grevesse (1989) solar ratios, close to the previously reported sub-solar abundance (e.g., REF). The effect of the simplistic model on the abundance measurement will be further discussed in section 4.

4.3. Abundance ratio of different heavy elements

In general, the relative abundance ratio of α-elements to *Fe* is roughly similar to the solar ratio. *Si* has the 2nd strongest (next to *Fe*) emission features. In contrast to *Fe*, its features are relatively isolated around ~2 keV and hence provide the most reliable measurement of α-element abundances. In Table 2 we list the results with all 4 different ways of grouping elements, which set to vary together. Although rather arbitrary, we intend to cover a range of methods used in the literature. Given the limited statistics and systematic and calibration uncertainties, we do not prefer one method to another, but simply present the possible range. The best-fit Z_{Si} ranges from 2 to 3 times solar within the D_{25} ellipse and decreases to ~1 solar outside the optical galaxy. Its ratio to *Fe* is close to solar and consistent to be solar in all cases in all radial bins, indicating no radial gradient of [*Si/Fe*]. This is consistent with the previous reports by Matsushita et al. (2000), although the absolute amount (Z_{Fe} or Z_{Si}) is considerably different. It is also consistent with the [*Si/Fe*] - *kT* relationship among galaxies and clusters (REF).

Abundance measurements of the other α-elements are not as reliable as Si. This is because their emission features are weaker and/or mixed with other features, and are possibly affected by calibration uncertainties. Also the measurement requires to set many fitting parameters to vary independently (**Z4** or Fit10 in Table 1 and 2).

The emission features of *S* is seen next to those of *Si* around E ~ 2.5 keV. They are also relatively isolated, but weaker than those of *Si*. The best-fit Z_S is slightly lower than *Fe* or *Si*. *S/Fe* is ~0.6 and barely consistent to be solar in the 90% confidence. No significant radial variation of *S/Fe* is evident.

The *Mg* emission features around E ~ 1.5 keV can be easily identified in the thermal gas with kT < 1 keV. However, *Fe* features start to blend with the *Mg* features in the hotter X-ray plasma with kT > 1 keV. Because the hot ISM in NGC 507 consists of multi-temperature mixtures of kT = 0.6-1.4 keV (see section 3.2), the measured amount of *Mg* could have some systematic effect, i.e., dependence on Z_{Fe}. The best-fit Z_{Mg} is slightly lower than *Fe* or *Si*. *Mg/Fe* is ~0.8, but consistent to be solar in the 90% confidence. Similar to Si and S, no significant radial variation of *Mg/Fe* is evident.

The emission features of *O* around E ~ 0.6-0.7 keV (or also ~0.5 keV for the colder plasma) are relatively isolated, but partially blend (at E ~ 0.7 keV) with the *Fe* features in the plasma with kT = 0.5 - 1 keV. In our spectral results, the best-fit *O/Fe* is lowest (0.3-0.5) among the measured α–elements within the D_{25} ellipse, while consistent to be solar at larger distances. The significance of difference is ~4σ in the 1st shell and ~3σ in the 2nd shell. The instrument calibration is least accurate at lower energies and the absorption could also affect the result. Given the uncertainties, although very intriguing, we consider the under-abundant O is suggestive, but not conclusive.

5. Discussions

The abundance of heavy elements has been identified as one of the key quantities for our understanding of the evolutionary status of the hot ISM in terms of the supernova rate (Type Ia and II), initial mass function (IMF), mass ejection and onset of galactic winds (e.g., Renzini et al. 1993, Matteucci and Gibson 1995). *Fe* exhibits the strongest X-ray emission features and therefore is the most commonly determined element with the X-ray spectra. The *Fe* abundance in the hot ISM is expected to be at least similar to (or higher than) that of the stellar population in elliptical galaxies, where Fe was initially synthesized by the bulk of Type II supernova (SN) explosions. Then, Type Ia SNe would continuously add heavy elements to the hot ISM. Therefore, the expected *Fe* abundance in the hot ISM is 2-5 times solar (see Arimoto et al. 1997).

In this paper, we present, for the first time, an unambiguous indication of super-solar *Fe* abundances, Z_{Fe} ~ 2-3 times solar with a maximum observational limit of 4-5 times solar. This is fully in agreement with the metal enrichment theory (e.g., Arimoto et al. 1997). To support our conclusion, we carefully consider various effects, which could affect the abundance measurement, as discussed in section 3. The most important factor is how to select the realistic emission model, i.e., how to untie model-abundance degeneracy. With the high quality XMM-Newton spectra, we have now enough statistics to rule out the simple models, which could result in a low-Z (as in Fit6 of Table 1). We further show that spatially (in 3-dimension) resolved, high quality XMM-Newton spectra require at

least 3-components, or 2 thermal components in addition to the hard LXMB component to represent localized temperature distribution inside the hot ISM.

In the following, we will discuss (1) what causes the multi-temperature gas, (2) how much the LMXB component present, and (3) whether extra absorption exists.

As discussed in section 3.2, the temperature of the hot ISM is not simply a function of radius. In addition to the overall temperature gradient (as seen in the ROSAT data in KF95), the hot ISM appears to consist of mixed gas with multi-temperatures within a concentric 3-dimensional shell. This could be explained by inhomogeneous, localized cooling which starts from the ambient gas of ~1.4 keV at large radii. We note that the central region NGC 507 exhibit rather complex sub-structures which could initiate the perturbation. Double peaks and a void in between, possibly related to the nuclear radio jet, are seen in the high resolution Chandra image (Forman et al. 2002). Also present are discontinuities of X-ray surface brightness toward NE (Kraft et al. 2003) and toward SW (Kim et al. in preparation). They are similar to a contact discontinuity or a cold front, which indicates recent mergers. In the cosmological simulations, a finite range of temperatures (as opposed to a single temperature) at a given radius is often found (e.g., Kawata and Gibson 2003). Therefore, it is clear that an overall radial temperature gradient alone does not reflect the real property of the hot ISM.

We find no thermal emission from gas cooler than $kT < 0.6$ keV (roughly ½ of the temperature in the ambient gas), as reported in other early type galaxies (REF). Some heating mechanisms (such as AGN feedback or thermal conduction) may compensate the cooling (REF). No cooling below the observed limit is sometimes used to argue against the multi-temperature model (REF). We note that this does not necessarily rule out the range of temperatures between that in the ambient gas (~1.4 keV) and the lower limit (~0.6 keV).

How much X-ray emission do we expect from the LMXBs in NGC 507? Chandra observations of giant elliptical galaxies often identify ~100 discrete sources, mostly LMXBs associated with the galaxies (e.g., ~150 in NGC 1399; Angelini et al. 2002). Because of the distance to NGC 507, typical LMXBs are not detected in our XMM-Newton observation and even in Chandra observations. The existing 16 ksec Chandra data (obsid=00317) found only 3 sources within the D_{25} ellipse (except the one in the center) and at the low s/n (see Kraft et al. 2003; also to be presented in our next paper). At the distance of 70 Mpc, typical LMXBs (with $L_X = 10^{37}$ - 10^{38} erg sec^{-1}) in NGC 507 would result in less than 1 count in the above Chandra observation. Only objects as bright as ULX (with $L_X > 10^{39}$ erg sec^{-1}) could be possibly detected. The total X-ray luminosity of undetected LMXBs can be indirectly determined by using its relationship with the optical luminosity. With a large sample of early type galaxies observed by Chandra, Kim and Fabbiano (2004) determined the relationship based on completeness-corrected X-ray luminosity function, i.e., with the measured detected LMXBs and estimated (by simulation) undetected LMXBs within the D_{25} ellipse:

$$L_X(\text{LMXB})/L(B) = 0.9 \pm 0.5 \times 10^{30} \text{ erg sec}^{-1} / L_\odot(B),$$

13

where we assume the XLF slope (α = ~1.0 in a cumulative form) continues down to L_X = 10^{37} erg sec^{-1}. We estimate L_X(LMXB) = 1.2 ± 0.7 x 10^{41} erg sec^{-1} for B_T° = 12.19 mag (taken from RC3), or F_X(LMXB) = 2.0 ± 1.1 x 10^{13} erg sec^{-1} cm^{-2}, which is ~2% (CHECK) of the total X-ray emission or ~10% of L_X within r < 40 kpc. The amount of the hard component determined by the spectral fitting is in agreement with the above estimation (Table 2). The best-fit normalization of the hard component (7 keV Bremsstrahlung) inside r < 2′ ranges between 2 to 3 x 10^{-13} erg sec^{-1} cm^{-2}. As discussed in section 3.2, a non-negligible amount of the hard component still remains at the outer shell (r = 60-100 kpc). The extra hard emission may originate from background AGNs, or those similar to the excess sources detected at larger distances (see Figure 1). Based on the Log(N)-Log(S) relationship determined in ChaMP (Kim et al. 2004), the expected background sources within the D_{25} ellipse of NGC 507 is less than 1 source, while several background sources could present in the outer shell to explain the hard emission.

The best-fit absorption (N_H = 6-7 x 10^{20} cm^{-2} in Fit7 of Table 1) is close the Galactic value (5 x 10^{20} cm^{-2}). Our estimate is consistent with the ROSAT results (**KF95**), but considerably lower than the ASCA results (1-2 x 10^{21} cm^{-2}), which suggest extra absorption (Matsumoto et al. 1997 and Matsushita, et al. 2000). Neither IRAS FIR (Knapp et al. 1989) nor HI observations (Knapp et al. 1985) of NGC 507 indicate significant internal absorption. A few x 10^{20} cm^{-2} within the D_{25} ellipse corresponds to M_{HI} ~10^{10} M$\odot$. With the observational upper limit of M_{HI} of 2.7 x 10^9 M$\odot$ (Knapp et al. 1985), we can rule out the presence of a significantly excess HI column density, internal to NGC 507. [However, see Arabadjis and Bregman (1999) for the possibility of an extra absorption by galactic molecular gas.] We note that N_H and the amount of the hard component are partially tied in a sense that a larger N_H tends to go with a smaller contribution from the hard component (and hence lower Z_{Fe}). This (another form of *spectral degeneracy*) occurs because the amount of absorption (more) and LMXBs (less) could change (reduce) model predictions in low (E < 0.7 keV) and high energies (E > 2 keV), respectively, i.e., effectively altering (reducing) the required strength of the Fe peak at ~1 keV. This could be partly responsible for the previous estimate of extremely low abundances.

The relative abundance of *Fe* and α-elements is critical information to discriminate the relative importance of SN type II and type Ia (e.g., Renzini et al. 1993; Loewenstein et al. 1994) and hence provides an important clue for the evolution of the hot ISM and the whole galaxy. If heavy elements are mainly synthesized in Type II SNe, the abundance ratio of α-elements to *Fe* is expected to be higher than the solar ratio (e.g., Woosley et al. 1995), while the ratio decrease as increasing contribution from Type Ia SNe (e.g., Iwamoto et al. 1999). In section 3.4, we show that the abundance ratio of *Si* to *Fe* is close to the solar ratio. Note that among α-elements the abundance measurement of *Si* is least uncertain because of its strong, isolated emission features and that the theoretical yields of *Si* is also best determined in a narrow range (e.g., Gibson et al. 1997; Nagataki & Sato 1998). With SN yields taken from Gibson et al. (1997) and converted to the revised solar values in Grevesse and Sauval (1998), the measured abundance ratio of *Si/Fe* (near solar) indicates a considerable contribution from SN Type Ia, i.e., 60-80% of the *Fe* mass is

originated from SN Type Ia. This in turn supports that Z_{Fe} is higher than the stellar *Fe* abundance. This is fully consistent with our finding of super-solar Z_{Fe}.

Based on the sub-solar *Fe* abundances estimated with ASCA spectra, it was suggested that SNe Type II dominate in young early-type galaxies and drive early galactic winds. This would imply a considerably flatter IMF (initial mass function) and less important SN Ia activity is required (e.g., Loewenstein et al. 1994; Mushotzky et al. 1994; Matsumoto et al. 1997), than had been assumed in these galaxies on the basis of stellar evolution models (e.g., Renzini et al. 1993; Arimoto et al. 1997). Our results indicate that those unusual constraints on IMF and/or SN Ia rate are not required.

S and *Mg* are found to be slightly less abundant (in the ratio to *Fe*) than *Si*, but still consistent with the solar ratio within the statistical error. *O* is least abundant among the measured α-elements. The under-abundant *O* (*O/Fe* lower than the solar ratio) is statistically significantly ($> 3\sigma$) within the D_{25} ellipse of the galaxy, while consistent to the solar ratio in the outskirts. Because both Type II and Type Ia produce similar amount of *Mg* and *O*, the apparent ratio of *O/Mg* which is considerably lower toward the center is hard to interpret. Buote et al. (2003b) reported a similar trend of the low *O* abundance in the center of NGC 5044 (similar to NGC 507 in both optical and X-ray perspectives) and suggested a warm absorber or an unknown physical/instrumental effect. Considering the various uncertainties discussed in section 3.4 (e.g., confusion with other emission features), the sub-solar Z_O (or *O/Mg* lower than the solar ratio) is suggestive, but not conclusive. Also we note that O carries a key (or mystery) to understand the fact that cooling apparently stops around 0.5-0.6 keV.

While we see a significant radial variation in metal abundances (both *Fe* and α-elements), the ratio of *Fe* to α-element abundances does not change, although large error bars (at large radii) allow a mild gradient (either positive or negative). This suggests that SNe Type II and Ia ejecta are relatively well mixed throughout the hot ISM.

6. Conclusion

After carefully analyzing high quality XMM-Newton spectra of X-ray bright early type galaxy NGC 507 and considering various systematic effects, we conclude the followings:

1. The Fe abundance is super-solar (2-3 times solar) within the optical galaxy. The allowed maximum is about 4 times solar. This is fully consistent with that expected by the stellar evolution models. The Fe abundance remains close to solar outside the optical galaxy, out to r = 100 kpc.

2. The α-element abundance abundances (mainly determined by Si) are also super-solar and the Fe to α-element abundance ratio is close to the solar ratio in all radii considered, indicating that SNe Type II and Ia ejecta are well mixed throughout the hot ISM. The Fe/Si ratio suggests that 60-80% of the *Fe* mass is originated from SN Type Ia.

15

Reference

Awaki et al, 1994, PASJ, 46, L65

Arimoto, N., Matsushita, K., Ishimaru, Y., Ohashi, T., and Renzini, A. 1997, ApJ, 477, 128

Brighenti, F., & Mathews, W. G. 1997, ApJ, 486, L83

Buote, D. A., Lewis, A. D., Brighenti, F., and Mathews, W. G. 2003a, ApJ in press (astro-ph/0205362)

Buote, D. A., Lewis, A. D., Brighenti, F., and Mathews, W. G. 2003b, ApJ, 595, 151.

Buote, D., and Fabian, A. C., 1998, ApJ, 296, 977.

David, L. P., Jones, C., Forman, W., & Daines, S. 1994, ApJ, 428, 544

Fabian, A. C. 1994, ARAA, 32, 277

Fabian, A. C., Nulsen, p. E. J., & Canizares, C. R. 1991, AA Rev. 2, 191

Fabbiano, G. 1989, ARAA, 27, 87

Huchra, J. P., Vogeley, M. S., & Geller, M. J. 1999, ApJS, 121, 287

Irwin, J. A., & Sarazin, C. L., 1998, ApJ, 494, L33

Kawata, D., & Gibbson, B. K. 2003, MNRAS in press (astro-ph/0308168)

Kim, D.-W., and Fabbiano, G., 1995, ApJ, 441, 182 (**KF95**)

Kim, D.-W., and Fabbiano, G., 2003, ApJ, 586, 826

Kim, D.-W., and Fabbiano, G., 2004, in preparation (LMXB paper)

Kim, D.-W., Fabbiano, G., & Trinchieri, G. 1992, ApJ 393, 134

Kim, D-W., Fabbiano, G., Matsumoto, H., Koyama, K., and Trinchieri, G. 1996, ApJ, 468, 175

Kim, D.-W. et al. 2004, ApJ, in press.

Kraft, R. P., Forman, W. R., Churazov, E., Laslo, N., Jones, C., Markevitch, M., Murray, S. S., Vikhlinin, A., 2003, submitted to ApJ.

Loewenstein, M., & Mathews, W. G. 1987, ApJ, 319, 614

Loewenstein, M., et al. 1994, ApJ, 436, L75.

Lumb, D. 2002, XMM-SOC-CAL-TN-0016 issue 2.0, http://xmm.vilspa.esas.es/external/xmm_sw_cal/calib

Matsumoto, H. et al. 1997, ApJ, 482, 133

Matsushita, K. et al. 1994, ApJ, 436, L41

Matteucci, F., and Gibson, B. K. 1995, AA, 304, 11

Mushotzky, M. et al. 1994, ApJ, 436, L79.

Nagataki, S., & Sato, K. 1998, ApJ, 504, 629

O'Sullivan, E.,

O'Sullivan, E.,

Paolillo, M., Fabbiano, G., Peres, G., & Kim, D.-W. 2003, ApJ, 586, 850

Renzini, A., Ciotti, L., D'Ercole, A., Pellegrini, S. 1993, ApJ, 419, 52.

Renzini, A. 1997, ApJ, 488, 35

Sarazin, C. L. 1988, ``X-ray Emissions from Clusters of Galaxies"

Sarazin, C. L., & White III, R. E. 1987, ApJ, 320, 32

Sarazin, C. L., & Ashe, G. A. 1989, ApJ, 345, 22

Sarazin, C. L. 1996 ``Galactic and Cluster Cooling Flows" ed. by Soker.

Snowden, S., Still, M., Harrus, I., Arida, M., & Perry, B. 2002, "An Introduction to XMM-Newton Data Analysis" version 1.3

Trinchieri, G., Kim, D.-W., Fabbiano, G., & Canizares, C. R. 1994, ApJ, 428, 555

Trinchieri, G., Fabbiano, G., & Kim, D.-W., 1997, AA, 318, 361

Vedder, P. W., Trester, J. J., Canizares, C. R. 1988, ApJ, 332, 725

```
                                          Table 1
--------------------------------------------------------------------------------------
      Method                  red_Ch2  (Ch2 / DoF)      Z(Fe)         error Z(Fe) in 90%
                                                       0'-1'  1'-2'    0'-1'      1'-2'
--------------------------------------------------------------------------------------

 <Fit1: template>

 BKL 3C 3D FNH  Z1 MOS1       1.05 (  578 /  554 )    2.56   1.82    1.7 - 3.8   1.2 - 2.4
 BKL 3C 3D FNH  Z1 MOS2       1.16 (  620 /  535 )    2.43   2.24    1.5 - 4.9   1.5 - 3.3
 BKL 3C 3D FNH  Z1 MOS12      1.17 ( 1296 / 1109 )    2.19   2.19    1.5 - 3.1   1.6 - 3.0
 BKL 3C 3D FNH  Z1 PN         1.21 ( 1731 / 1428 )    3.67   2.32    2.3 - 5.7   1.8 - 3.1
 BKL 3C 3D FNH  Z1 MOSPN      1.21 ( 3092 / 2557 )    2.85   2.16    2.2 - 3.8   1.8 - 2.6

 <Fit2 Fit3: different background>

 BKE 3C 3D FNH  Z1 MOS1       1.37 (  758 /  554 )    1.99   1.61
 BKE 3C 3D FNH  Z1 MOS2       1.83 (  977 /  535 )    1.58   1.58
 BKE 3C 3D FNH  Z1 MOS12      1.68 ( 1862 / 1109 )    1.98   1.65
 BKE 3C 3D FNH  Z1 PN         1.53 ( 2184 / 1428 )    2.45   2.08
 BKE 3C 3D FNH  Z1 MOSPN      1.67 ( 4269 / 2557 )    2.00   1.79

 BKB 3C 3D FNH  Z1 MOS1       1.19 (  658 /  554 )    2.31   1.81
 BKB 3C 3D FNH  Z1 MOS2       1.31 (  703 /  535 )    2.22   2.32
 BKB 3C 3D FNH  Z1 MOS12      1.29 ( 1430 / 1109 )    2.32   2.08
 BKB 3C 3D FNH  Z1 PN         1.22 ( 1742 / 1428 )    4.08   2.28
 BKB 3C 3D FNH  Z1 MOSPN      1.27 ( 3248 / 2557 )    3.54   2.08

 <Fit4: different emission model>

 BKL 2C 3D FNH  Z1 MOS1       1.35 (  728 /  539 )    1.19   1.19
 BKL 2C 3D FNH  Z1 MOS2       1.23 (  684 /  558 )    1.50   0.93
 BKL 2C 3D FNH  Z1 MOS12      1.36 ( 1509 / 1113 )    1.33   1.06
 BKL 2C 3D FNH  Z1 PN         1.44 ( 2060 / 1432 )    2.34   1.13
 BKL 2C 3D FNH  Z1 MOSPN      1.43 ( 3670 / 2561 )    1.43   1.05

 <Fit5, Fit6: without de-projection>

 BKL 3C 2D FNH  Z1 MOS1       1.04 (  577 /  554 )    1.93   1.34    1.6 - 2.5   1.2 - 1.7
 BKL 3C 2D FNH  Z1 MOS2       1.16 (  619 /  535 )    1.94   1.49    1.6 - 2.3   1.3 - 1.8
 BKL 3C 2D FNH  Z1 MOS12      1.17 ( 1293 / 1109 )    1.92   1.45    1.6 - 2.3   1.3 - 1.7
 BKL 3C 2D FNH  Z1 PN         1.21 ( 1729 / 1428 )    2.32   1.56    2.1 - 2.7   1.5 - 1.7
 BKL 3C 2D FNH  Z1 MOSPN      1.21 ( 3094 / 2557 )    2.13   1.49    1.9 - 2.3   1.5 - 1.5

 BKL 2C 2D FNH  Z1 MOS1       1.33 (  741 /  558 )    1.10   0.74
 BKL 2C 2D FNH  Z1 MOS2       1.43 (  769 /  539 )    1.03   0.81
 BKL 2C 2D FNH  Z1 MOS12      1.44 ( 1604 / 1113 )    1.06   0.78
 BKL 2C 2D FNH  Z1 PN         1.55 ( 2218 / 1432 )    1.12   0.82
 BKL 2C 2D FNH  Z1 MOSPN      1.51 ( 3880 / 2561 )    1.09   0.80

 <Fit7: varying N(H)>

 BKL 3C 3D VNH  Z1 MOS1       1.03 (  569 /  553 )    2.34   1.37    1.4 - 3.8   0.9 - 1.8
 BKL 3C 3D VNH  Z1 MOS2       1.14 (  610 /  534 )    2.08   1.37    1.4 - 3.3   1.2 - 2.1
 BKL 3C 3D VNH  Z1 MOS12      1.15 ( 1275 / 1108 )    1.98   1.49    1.5 - 2.4   1.2 - 1.7
 BKL 3C 3D VNH  Z1 PN         1.19 ( 1690 / 1427 )    2.47   1.51    2.3 - 3.0   1.4 - 1.7
 BKL 3C 3D VNH  Z1 MOSPN      1.19 ( 3037 / 2556 )    2.03   1.47    1.9 - 2.4   1.4 - 1.6

 <Fit8 Fit9 Fit10: differrent groups of elements to vary>

 BKL 3C 3D FNH  Z2 MOS1       1.05 (  578 /  550 )    2.87   1.75    1.8 - 3.7   1.4 - 2.4
 BKL 3C 3D FNH  Z2 MOS2       1.17 (  619 /  531 )    2.39   2.20    1.6 - 4.4   1.5 - 4.6
 BKL 3C 3D FNH  Z2 MOS12      1.17 ( 1294 / 1105 )    2.29   2.05    1.6 - 3.5   1.5 - 2.8
 BKL 3C 3D FNH  Z2 PN         1.20 ( 1712 / 1424 )    3.67   2.41    3.3 - 4.8   2.1 - 2.8
 BKL 3C 3D FNH  Z2 MOSPN      1.21 ( 3085 / 2553 )    3.23   2.16    2.1 - 4.2   1.8 - 2.7

 BKL 3C 3D FNH  Z3 MOS1       1.04 (  570 /  550 )    2.19   1.68    1.6 - 4.2   1.1 - 2.6
 BKL 3C 3D FNH  Z3 MOS2       1.12 (  596 /  531 )    1.76   1.90    1.2 - 2.5   1.2 - 3.3
 BKL 3C 3D FNH  Z3 MOS12      1.15 ( 1267 / 1105 )    1.99   1.97    1.5 - 2.9   1.4 - 2.4
 BKL 3C 3D FNH  Z3 PN         1.17 ( 1665 / 1424 )    2.69   2.00    1.8 - 3.5   1.5 - 2.3
 BKL 3C 3D FNH  Z3 MOSPN      1.18 ( 3005 / 2553 )    2.49   1.83    2.1 - 3.0   1.6 - 2.5

 BKL 3C 3D FNH  Z4 MOS1       0.96 (  519 /  538 )    1.89   1.39    1.1 - 3.6   1.0 - 2.0
 BKL 3C 3D FNH  Z4 MOS2       1.03 (  535 /  519 )    1.35   1.49    1.0 - 1.9   1.0 - 2.1
 BKL 3C 3D FNH  Z4 MOS12      1.07 ( 1165 / 1093 )    1.55   1.44    1.1 - 2.1   1.1 - 2.0
 BKL 3C 3D FNH  Z4 PN         1.17 ( 1645 / 1412 )    2.17   1.92    1.6 - 3.0   1.6 - 2.5
 BKL 3C 3D FNH  Z4 MOSPN      1.15 ( 2913 / 2541 )    1.71   1.70    1.5 - 2.1   1.5 - 2.1


 <5-shells>
 <He>
--------------------------------------------------------------------------------------
```

Note. codes used in methods:

1st column - instrument
   MOS1, MOS2 and PN: fitting individually
   MOS12: fitting jointly for MOS1 + MOS2
   MOSPN: fitting jointly for MOS1 + MOS2 + PN

2nd column - background spctra
   BKL: background spectra are taken from the local region (see Figure 2)
   BKE: background spectra are taken from the edge of the field of view (see Figure 2), then scaled by arf
   BKB: background spectra are taken from the blank field, then scaled by counts in the BKL region

3rd column - emission models
   2C: 2-component model, 1 soft thermal (vmekal) + 1 hard (7 keV bremsstrahlung)
   3C: 3-component model, 2 soft thermal (vmekal + 1.4 keV vmekal) + 1 hard (7 keV bremsstrahlung)

4th column - projection
   2D: no de-projection
   3D: projection of 3-dimensional models and compare with data

5th column - grouping elements
   Z1: all heavy elements vary together
   Z2: Si and S vary together and the other elements vary with Fe
   Z3: elements lighter than Ca vary together and the rest elements vary with Fe
   Z4: Fe, Si, S, Mg and O vary independently and the rest elements vary with Fe

6th column - NH
   FHN: N(H) is fixing at the galactic value (5×10^{20} cm^-2)
   VNH: N(H) is free to vary

Table 2. Radial variations of spectral parameters

	r=0-1′		r=1-2′		r=2-3′		r=3-5′	

3-component models:

\<Z1 – Fit1\>

T(1)	0.82	(0.79 – 0.84)	0.78	(0.75 – 0.80)	0.71	(0.65 – 0.78)	0.63	(0.54 – 0.73)
Fx(1)	5.25	(3.48 – 6.89)	4.26	(3.47 – 5.33)	0.83	(0.56 – 1.10)	0.81	(0.50 – 0.98)
Fx(2)	6.75	(4.86 – 8.71)	12.62	(10.57 – 14.93)	11.03	(9.09 – 12.12)	13.08	(11.63 – 14.85)
Fx(3)	0.82	(0.07 – 1.49)	1.43	(0.83 – 2.05)	0.91	(–)	2.77	(1.66 – 3.64)
Fe	2.85	(2.23 – 3.79)	2.16	(1.80 – 2.58)	1.03	(0.92 – 1.27)	0.71	(0.62 – 0.82)

\<Z2 – Fit8\>

T(1)	0.81	(0.79 – 0.84)	0.78	(0.74 – 0.81)	0.71	(0.60 – 0.81)	0.64	(0.54 – 0.73)
Fx(1)	5.18	(3.84 – 7.95)	4.16	(3.31 – 5.22)	0.79	(0.50 – 1.08)	0.82	(0.50 – 1.16)
Fx(2)	6.75	(5.07 – 9.78)	12.60	(10.41 – 15.08)	11.01	(8.67 – 11.99)	12.96	(11.63 – 14.85)
Fx(3)	0.90	(0.15 – 1.62)	1.57	(0.92 – 2.19)	0.97	(–)	2.94	(1.90 – 3.87)
Fe	3.23	(2.15 – 4.21)	2.16	(1.82 – 2.65)	1.00	(0.91 – 1.25)	0.72	(0.62 – 0.83)
Si	3.30	(2.75 – 3.83)	1.94	(1.63 – 2.28)	0.89	(0.70 – 1.16)	0.70	(0.54 – 0.86)

\<Z3 – Fit9\>

T(1)	0.81	(0.78 – 0.84)	0.77	(0.72 – 0.80)	0.71	(0.56 – 0.82)	0.59	(0.51 – 0.76)
Fx(1)	4.76	(3.37 – 6.68)	3.78	(2.93 – 4.64)	0.72	(0.40 – 1.03)	0.77	(0.47 – 1.13)
Fx(2)	7.07	(4.90 – 9.67)	12.84	(10.17 – 15.19)	10.90	(8.52 – 12.21)	12.55	(11.64 – 15.59)
Fx(3)	1.03	(0.19 – 1.73)	1.77	(1.05 – 2.57)	1.21	(–)	3.56	(1.80 – 4.41)
Fe	2.49	(1.83 – 3.53)	1.83	(1.55 – 2.31)	0.97	(0.86 – 1.29)	0.77	(0.61 – 0.84)
Si	1.90	(1.53 – 2.62)	1.32	(1.03 – 1.80)	0.78	(0.60 – 1.14)	0.65	(0.44 – 0.77)

\<Z4 – Fit10\>

T(1)	0.79	(0.76 – 0.82)	0.74	(0.71 – 0.78)	0.71	(0.55 – 0.80)	0.58	(0.51 – 0.73)
Fx(1)	4.82	(3.28 – 5.72)	3.73	(3.01 – 4.70)	0.72	(0.23 – 1.02)	0.75	(0.47 – 1.09)
Fx(2)	7.28	(5.00 – 8.62)	13.07	(10.92 – 15.50)	11.00	(8.90 – 12.63)	12.95	(11.23 – 15.04)
Fx(3)	0.67	(– 2.01)	1.52	(0.77 – 2.26)	1.07	(– 9.07)	2.98	(1.20 – 4.00)
Fe	1.71	(1.48 – 2.14)	1.70	(1.45 – 2.07)	0.97	(0.84 – 1.23)	0.71	(0.60 – 0.78)
Si	1.85	(1.56 – 2.11)	1.64	(1.37 – 1.96)	0.92	(0.68 – 1.21)	0.81	(0.62 – 1.01)
S	1.06	(0.61 – 1.52)	1.01	(0.67 – 1.39)	0.75	(0.44 – 1.10)	0.46	(0.22 – 0.69)
Mg	1.69	(1.25 – 2.15)	1.32	(0.94 – 1.76)	0.56	(0.13 – 1.02)	0.62	(0.28 – 0.96)
O	0.53	(0.24 – 0.85)	0.82	(0.55 – 1.17)	0.71	(0.33 – 1.07)	0.61	(0.34 – 0.94)

Two-component models:

\<3D – Fit4\>

T(1+2)	0.99	(0.97 – 1.01)	1.03	(1.02 – 1.04)	1.41	(1.38 – 1.43)	1.41	(1.38 – 1.43)

\<2D – Fit6\>

T(1+2)	1.03	(1.03 – 1.04)	1.10	(1.09 – 1.11)	1.37	(1.35 – 1.39)	1.40	(1.38 – 1.43)

Figure 1: XMM-Newton true-color X-ray image of NGC 507. Combined MOS1 + MOS2 image is smoothed with gaussian sigma=7.5′ with red for the soft band in 0.3-0.9 keV, green for the medium band in 0.9-2.5 keV and blue for the hard band in 2.5-8.0 keV. North is to the top and east is to the left.
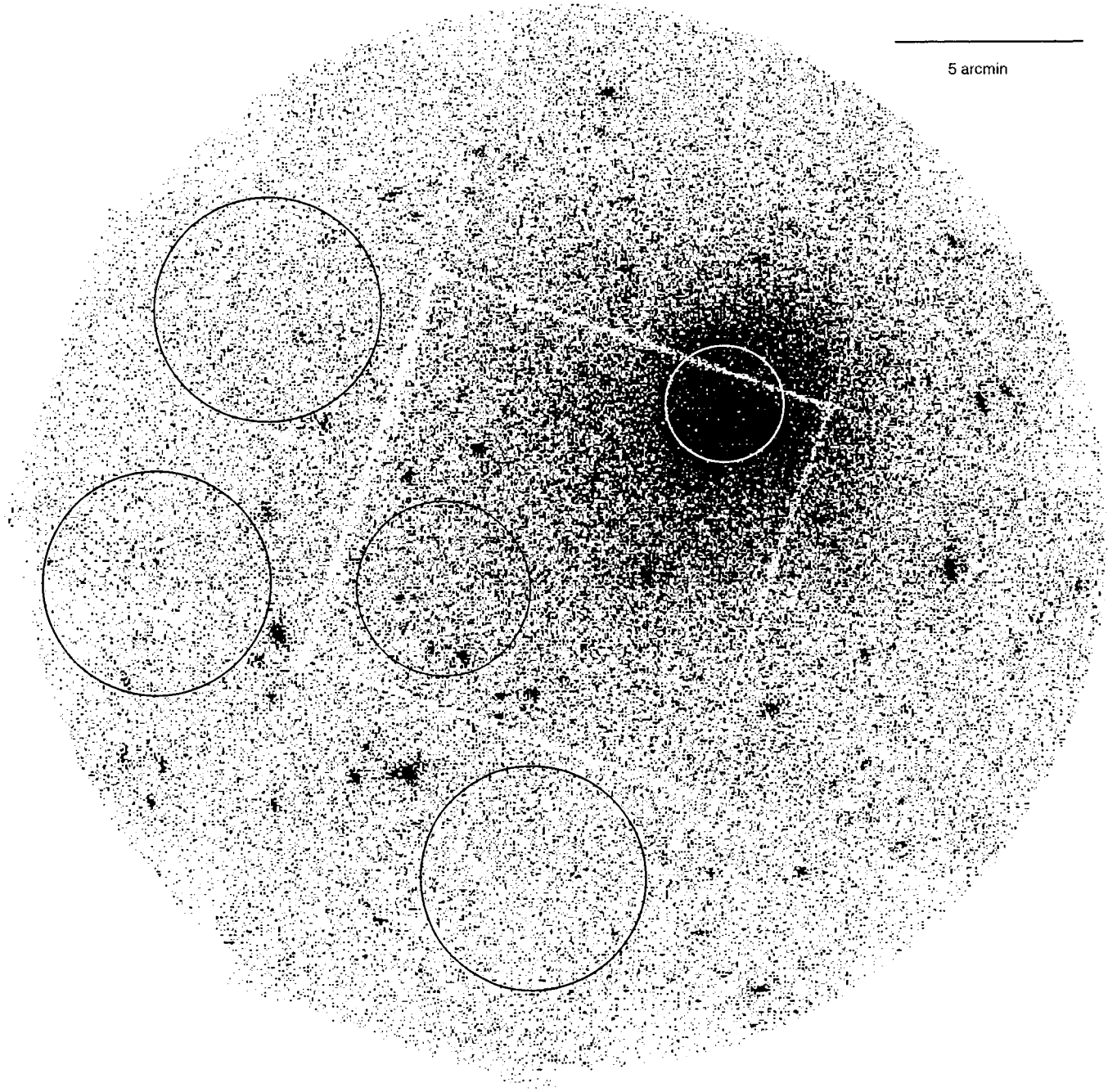
5 arcmin

Figure 2: XMM-Newton (unsmoothed) image. The D_{25} ellipse is marked. Also marked are regions where 3 sets of background spectra are extracted. The local background is taken from the cyan circle near the aim point and the second background is taken from the 3 big blue circles near the edge of the field of view. Also blank field data are used after scaling counts in the above background regions (see text for more details). North is to the top and east is to the left.
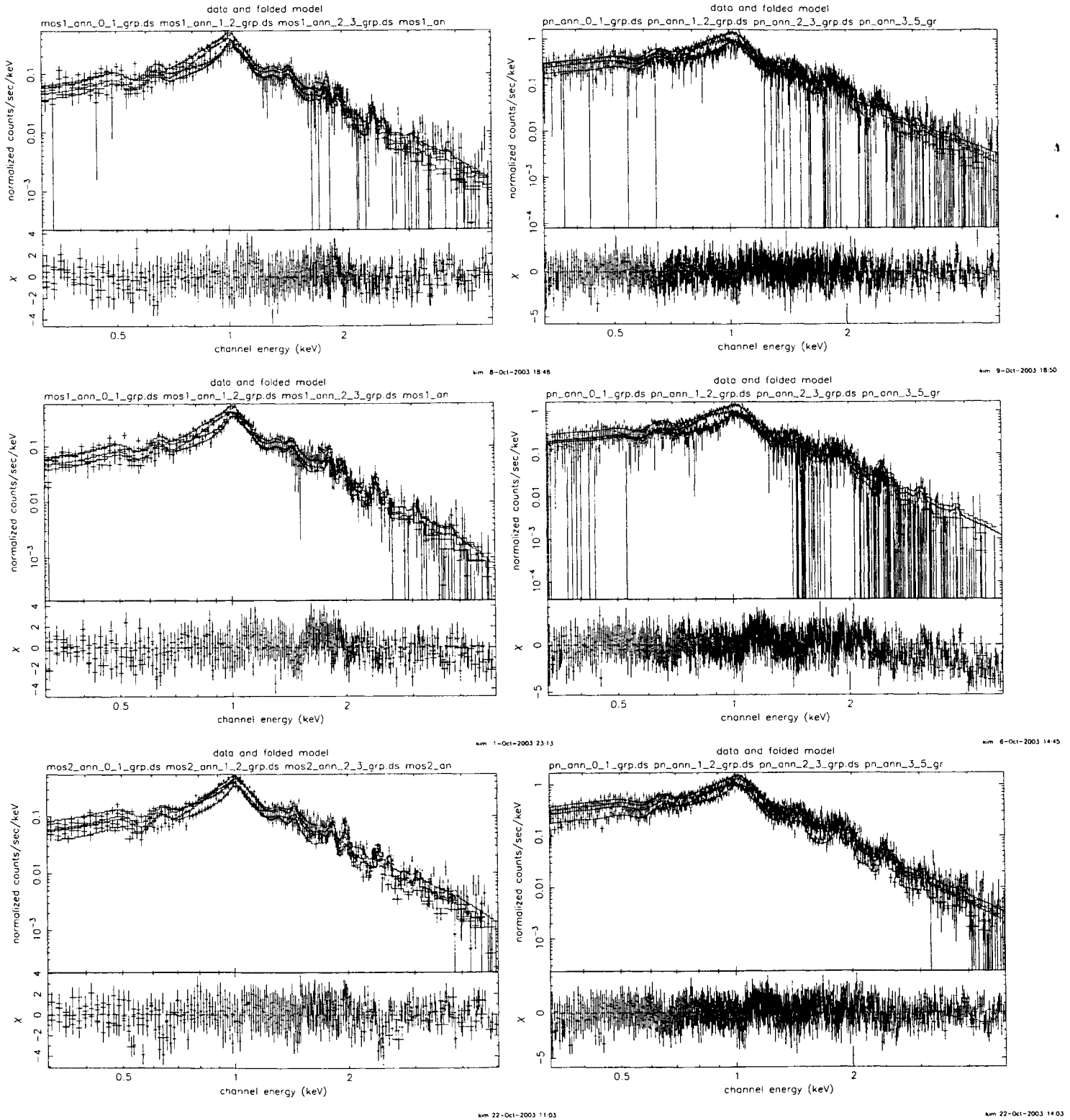
Figure 3: Comparison of spectral fitting with 3 different sets of background spectra. (a, b) MOS1 and PN spectra are extracted from 4 concentric annuli and subtracted by the local background spectra obtained near the aim point. They are then fitted with projected 3-dimensional models with 3 components (2 soft thermal components with 2 different temperatures and 1 hard component). All the heavy elements vary together (although independently in different shells) and N_H is fixed at the galactic value. (c, d) same as (a b) except the background spectra are taken from the edge of the field of view and re-scaled by arf at $E < 5$ keV. (e, f) same as (a b) except the background spectra are taken from the blank field data and re-scaled by the ratio of counts taken from the local bakground region at $E = 5$ - 10 keV.